A Wideband IF Receiver Chip for Flexibly Scalable mmWave Subarray Combining and Interference Rejection

Rehman Akbar, *Graduate Student Member, IEEE,* Eric A. M. Klumperink, *Fellow, IEEE,* Nuutti Tervo, *Member, IEEE,* Kari Stadius, *Member, IEEE,* Timo Rahkonen, *Member, IEEE* Aarno Pärssinen, *Senior Member, IEEE*

***Abstract*—Large-scale multi-beam phased array systems suffer from inter-beam interference that should be canceled either in the analog or digital domain. In wideband systems such as fifth generation (5G), interference rejection over a wide bandwidth is challenging to achieve, not only due to non-idealities of the receiver chain but also due to the properties of the radio channel. This article presents a scalable inter-beam interference cancellation (IBIC) scheme at intermediate frequency (IF) using an IF receiver (IF-RX) chip. The IF-RX provides the flexibility of not just interference rejection between the subarrays but also wideband signal combining over multiple subarrays. It also provides wideband filtering before the analog-to-digital converter (ADC) to support 5G channel bandwidths of up to 800 MHz, high linearity and low noise figure. A calibration method is proposed to find the cancellation coefficients for the IF receiver in measurements. Furthermore, a simplified over-the-air (OTA) IBIC model for analyzing rejection bandwidth limitations is presented. Interference rejection performance is demonstrated through the OTA measurements using 5G new radio (5G NR) signals. In the OTA measurements, 34–37-dB of rejection was achieved for 50–100-MHz signals, while error vector magnitude (EVM) requirements of the 5G standards were met with good margins. Finally, the interference rejection over 4×100 MHz carrier aggregated 5G NR waveform was demonstrated.**

***Index Terms*—Beamforming, complex multiplication, inter-beam interference cancellation (IBIC), phase shifter, phased array.**

I. Introduction

FIFTH-generation (5G) communication utilizes large-scale phased arrays to enhance the signal-to-noise ratio (SNR), link budget and spatial selectivity at millimeter-wave (mmWave) frequencies [1]. Large-scale phased array systems utilize a subarray approach to provide flexibility and scalability in system design based on specific link budget requirements. These subarrays can then be used in a variety of ways: signal contributions can be summed to increase beamforming gain [2]–[6] or used in a multibeam phased array system by assigning each subarray to a single user [7]. Each subarray user beam may experience interbeam interference. In particular, when an unwanted beam falls close to the main-lobe or sidelobe maximum, interference may exceed the desired signal before digitization, resulting in high dynamic range analog-to-digital converter (ADC) requirements [8], [9]. As a result, it is critical to provide IBIC in the analog domain to improve the signal-to-interference-plus-noise ratio (SINR) before the ADC to relax dynamic range and thus power consumption as motivated in [10] and demonstrated in this article.

Recent works [3], [4], [11] focus on combining signals from multiple subarrays at intermediate frequency (IF) and exploit orthogonal polarization to increase the channel capacity by creating independent user beams. However, in the presence of multiple users within the same polarization, interference cancellation is required to achieve a decent SINR and data rate for all beams under various user conditions. Active interference cancellation can be realized, for example, by creating the null/notch in the direction of an interferer in the spatial domain by a feedforward cancellation path or by using zero-forcing techniques in the digital domain after the ADC. In addition, any combination of different digital and analog techniques can be used. To maximize the capacity and frequency reuse, this should be done over the entire bandwidth of the whole receiver.

For 5G new radio (5G NR) sub-6-GHz or mmWave systems having radio frequency (RF) bandwidths of hundreds of MHz, wide cancellation bandwidth is required. In [12], adaptive null steering is achieved in an mmWave multi-input-multi-output (MIMO) receiver by directly employing mmWave transconductor currents for phase shifting. However, null steering in one direction requires antenna-specific amplitude control and it may potentially increase the interference in other directions. Alternatively, Huang and Wang [13] proposed beamforming and multi-stage interference rejection at an IF of 2–5 GHz. Narrow-band phase shifters are used for beamforming and the cancellation paths employ tunable passive delay lines and variable-gain amplifiers (VGAs) to achieve wide rejection bandwidth and compensation of path differences. However,

Manuscript received 10 March 2023; revised 1 May 2023; accepted 16 May 2023. This research has been supported in part by Academy of Finland Ex5GRx under Grant 2430226211 and in part by Academy of Finland, 6G Flagship program under Grant 346208.

Rehman Akbar, Nuutti Tervo, and Aarno Pärssinen are with the Cen- ter for Wireless Communications–Radio Technologies, University of Oulu, 90570 Oulu, Finland (e-mail: rehman.akbar@oulu.fi).

Eric A. M. Klumperink is with the IC Design Group, Faculty of Electrical Engineering, Mathematics, and Computer Science, University of Twente, 7500 AE Enschede, The Netherlands.

Kari Stadius is with the Department of Electronics and Nano Engineering, Aalto University, 00076 Espoo, Finland.

Timo Rahkonen is with the Circuit and System Group, Faculty of Information Technology and Electrical Engineering, University of Oulu, 90570 Oulu, Finland.

Color versions of one or more figures in this article are available at https://doi.org/10.1109/TMTT.2023.3279919.

Digital Object Identifier 10.1109/TMTT.2023.3279919

the implementation of passives with large area penalty makes it less attractive for low-GHz frequencies. In [14], a two-stage fully connected subarray architecture that performs zero forcing in the digital domain is demonstrated. However, this increases the number of required ADCs and increases their dynamic range requirements. On the other hand, the cancellation at RF, implemented at the low noise amplifier (LNA) output in [15] at 10 GHz, requires band-limiting quadrature hybrids, degrading the receiver noise performance and providing narrow-band interference cancellation.

In MIMO receivers operating in the sub-6-GHz bands, recent papers have focused on spatial notch filtering approaches [16]–[20]. Two stages of the interference cancellation are proposed in [16] based on a spatial notch filter and feedforward cancellation path realized in the voltage domain at baseband (BB), which results in limited bandwidth of the notch rejection and linearity. An improvement of the notch bandwidth and linearity is demonstrated in [17] by exploiting current-mode passive mixer avoiding large voltage swing at the mixer output to improve the linearity. Golabighezelahmad [18] demonstrates wideband interference rejection and high linearity by the slicing of RF transconductors using directly the currents to provide phase shift by steering the current with static reconfiguration switches to low-ohmic, wideband transimpedance amplifier (TIA) nodes. Alaei et al. [19] demonstrated adaptive interference rejection both in analog and digital domains and includes OTA measurements using vector modulator (VM) of [18] for RF frequencies up to 6-GHz and narrowband (1 MHz) signals.

This article presents a broadband mmWave subarray-based architecture concept for spatial filtering and IBIC to improve the SINR between independent beams using multiple wideband IF receiver (IF-RX) chips [21]. Compared with [21], this work further investigates the performance of the proposed architecture concept for wideband IBIC using the IF-RX in the presence of circuit matching and OTA channel nonidealities. This article also analyzes the limitations of the interference rejection bandwidth (BW_{Canc}) caused by nonidealities in the circuit and in the OTA channel. Furthermore, we also propose a calibration method to find the cancellation weights based on the power and error vector magnitude (EVM) measurements.

System considerations are discussed in Section II. The IF-RX chip architecture and circuit details are shown in Section III, proposing flexible summation of parallel IF-RX paths either for improved directivity or interference rejection. Section IV discusses the factors affecting the rejection precision, concentrating on the delay mismatch impact due to the OTA channel between two antenna signals. Compared with [21], Section V shows additional measurements of IF-RX, and Section VI illustrates the rejection performance up to 400 MHz in OTA measurements with modulated orthogonal frequency-division multiplexing (OFDM) signals used in the 5G NR standard. The performance is compared against the state-of-the-art. Finally, Section VII concludes the work.

II. SYSTEM CONSIDERATIONS

A common approach in a multibeam system is to have a dedicated subarray for each user that can be physically separated. Each subarray performs analog beamforming by directing the beams toward one specific user that transmits one data stream, spatially filtering out-of-beam interferers, and downconverting the mmWave signal to IF or BB, as shown in Fig. 1(a). While every subarray provides spatial filtering, each beam may still experience relatively high sidelobe levels (SLLs), resulting in limited spatial filtering and thus SINR from beams coming from other directions. Furthermore, the received signals may have different power levels especially in multi-user scenarios, leading to even higher interbeam interference. An additional interference rejection scheme is then required to improve the SINR for all the received beams.

In this article, IBIC is performed in the analog domain at IF to receive multiple independent data streams while improving the SINR of each beam using the IF-RX chip of [21]. The architecture of the IF-RX chip, shown in Fig. 2, provides the following functions: 1) vector modulation; 2) cartesian combining of two input signals; 3) zero-IF downconversion; and 4) low-pass filtering for channel selection. Based on this IF-RX chip, two architectures are proposed for IBIC, as shown in Fig. 1(b) and (c), considering a two-user scenario. Fig. 1(b) shows the IBIC scheme with mmWave subarrays, which applies the complex beamforming weights at mmWave before downconversion to IF. The complex weighted signals of each antenna element in each mmWave subarray are summed at mmWave and downconverted to IF, providing single voltage output $V_{C\sum}$ (sum of signals after complex weighting). Here, the IF-RX chip works as a VM to realize IBIC at IF. Fig. 1(c) shows IBIC for a Cartesian combining architecture. Here, each antenna element splits into two paths named real and imaginary path, provides scalar-only beamforming weights with VGAs named $Ar_{1\text{-}n}$ and $Ai_{1\text{-}n}$ (amplitude weights for real and imaginary) at mmWave [22]. The scalar-only weighted signals of each path are summed at mmWave and downconverted to IF, providing $V_{Ar\sum}$ and $V_{Ai\sum}$ voltage outputs, respectively. Cartesian combining ($V_{Ar\sum}$+j$V_{Ai\sum}$) is implemented in the IF-RX chip that implements the 90° phase shifting, which can be done more accurately at the lower IF-frequency. The I/Q generation at low-IF can be done by using digital dividers, which can have a large tunning range, driving I/Q mixers to realize 90° phase shift. This avoids the generation of 90° phase shift for each antenna element over a broad range of mmWave frequencies [22], [23]. It relaxes the mmWave subarray design that is already challenging and now only needs mixers and VGAs, not phase shifters. On the other hand, the potential challenge for the architecture of Fig. 1(c) is high mixer linearity because the quadrature combining for beamforming is realized after mixing, as a result exposing mixers to potentially stronger interferers.

In both architectures shown in Fig. 1(b) and (c), the mmWave subarray module optimizes the SNR of the receiver, realize the spatial filtering of mutual interference between user1 and user2, and reduces the magnitude of possible multipath reflections from different directions. Thus, prior to the IBIC, mmWave spatial filtering offers wideband signal rejection. The IBIC scheme requires amplitude matching and phase rotation such that the user2 signal is canceled in the user1 path and vice versa. To this end, each mmWave subarray

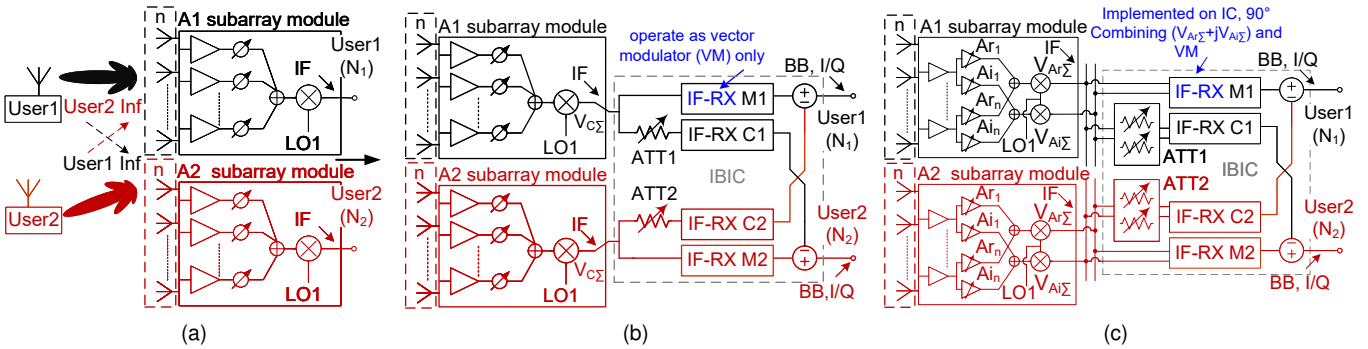

Fig. 1. (a) Sub-array per user approach with the cross-user inter-beam interference(IBI). (b) Proposed dual-stage mmWave phased array architecture for a large sub-array receiver with parallel IF-RXs working as VM used in the main path (M) and cancellation/combining path (C) to realize IBIC. (c) The same IF-RX chip used to support a mmWave cartesian combining architecture.

IF output is split into an IF-RX main path (M) and a combining or cancellation path (C) as shown in Fig. 1(b) and (c). The IF-RX M1 and M2 paths receive user1 and user2 streams and provide channel selection filtering for wideband signals. IF-RX C1 and C2 paths can be used for combining signals of multiple subarrays implemented on separate modules/ICs into one BB output or as interference cancellation paths, as studied in this article using the architecture shown in Fig. 1(b).

The dual-conversion IBIC scheme exploits the constant-gm VM concept [24], previously used for interference rejection in zero-IF MIMO receivers [18]. Although similar in circuit topology, the system and circuit requirements are quite different. In a low-GHz array with a limited number of antenna elements (4×4 MIMO) [18], [19], it is feasible to realize programmable complex weights for each antenna element. This becomes unpractical for mmWave arrays that require much more antenna elements. In this work, each IF-RX chip accesses already weighted and summed mmWave signals to reduce the number of IF signals to two per mmWave subarray ($V_{Ar\sum}$ and $V_{Ai\sum}$). The number of IF-RX chips depends on the number of data streams (Ns) and not the number of antennas. To enable IBIC, Ns data streams require one IF-RX chip in the main path and (Ns-1) cancellation paths at the output of each mmWave subarray. In addition, each cancellation path uses attenuators (ATT) in front of the VM to broaden the achievable dynamic range, whereas work [18] relies on the VM only for amplitude and phase matching when synthesizing beam patterns with arbitrary nulls. Thus, it loses phase resolution when main and cancellation path signal levels have a large amplitude difference. This work uses ATTs to do the amplitude matching and operate the VM in the maximum phase resolution, thus providing better rejection. It allows the VM to achieve 26-dB of rejection with 5-bit phase quantization [25].

In scenarios with less interference, some cancellation paths can be redundant. They can still be useful to improve the signal quality by combining multiple subarrays into one BB output when subarray beams point to the same user. The rest can be utilized for cancellation. This approach provides the flexibility of scaling and selecting the mmWave subarrays and the number of data streams. To be effective, the IF-RX chip for mmWave 5G NR system should feature: 1) large BB bandwidth to process wideband signals available at mmWave; 2) moderate noise figure (NF) after subarray combining; 3) good linearity to handle the combined signal dynamics; and 4) the capability of interference rejection over a wide bandwidth.

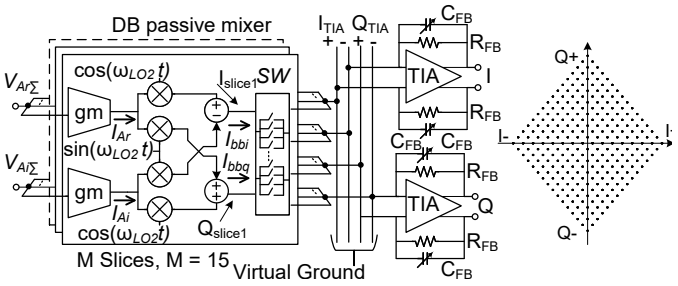

Fig. 2. IF receiver (IF-RX) chip architecture. The current combining at the output is done by a baseband transimpedance amplifier (BB-TIA).

III. IF-RX Module

The constant-gm VM was originally proposed with capacitive voltage output in [24] and with TIA output designed for zero-IF MIMO in [18]. Here we modify it to perform Cartesian combining (90° phase shift) and a VM function compatible with the mmWave subarrays. Hence, unlike [18] where each antenna provides a single-wire (real) input signal to the VM, here we need to support a two-wire input signal to realize complex signal, $V_{Ar\sum}$+j$V_{Ai\sum}$ as depicted in Fig. 1(c). The 90° phase shift to realize cartesian combining is implemented in IF-RX exploiting quadrature mixing as shown in Fig. 2.

A. VM Function

The architecture of the IF-RX chip is shown in Fig. 2. It uses a low-noise transconductance amplifier (LNTA) for *V-I* conversion and downconverts the IF between 2 and 4 GHz to BB. The VM function is realized by dividing the IF-RX into parallel slices (amplitude weighing) while varying the phase with a selection block implemented by static phase selection switches in each slice (”SW” in Fig. 2) [24]. Instead of exploiting charge sharing on a capacitor averaging the output as in [24], Cartesian combining is implemented by

current summing into a virtual ground node provided by a transimpedance amplifier (TIA) as shown in Fig. 2.

The Cartesian combining and VM functionality can be understood by calculating signals at different nodes of the IF-RX. Consider the voltage input signal is represented in terms of its complex envelope $\tilde{x}(t)$ then the real and imaginary paths' sum terms can be given as $V_{Ar\sum}(t) = Ar_{\sum}\ \tilde{x}(t)\cos(\omega_H t)$ and $V_{Ai\sum}(t) = Ai_{\sum}\ \tilde{x}(t)\cos(\omega_H t)$. Those are split into binary weighted slices, and each unit slice contains constant gm stage and double-balanced passive quadrature mixing. The gm-stage converts IF input voltage to current i.e., $I_{Ar\sum} = gmV_{Ar\sum}$ and $I_{Ai\sum} = gmV_{Ai\sum}$. Assuming low impedance at the TIA input node, this current is downconverted to BB by the four-phase double-balanced passive mixer. The BB current $I_{bbi}(t)$ at node I_{slice} can be written as

$$\frac{2\sqrt{2}}{\pi\ M}\tilde{x}(t)gm\left((Ar_{\sum} - jAi_{\sum})e^{j\omega_{bb}t} + (Ar_{\sum} + jAi_{\sum})e^{-j\omega_{bb}t}\right) \tag{1}$$

and BB current $I_{bbq}(t)$ at node Q_{slice} as

$$\frac{2\sqrt{2}}{\pi\ M}\tilde{x}(t)gm\left((Ai_{\sum} + jAr_{\sum})e^{j\omega_{bb}t} + (Ai_{\sum} - jAr_{\sum})e^{-j\omega_{bb}t}\right) \tag{2}$$

where M is the number of slices, $\omega_{bb} = \omega_H - \omega_{LO}$ and $2\sqrt{2}/\pi$ is the magnitude of current in BB. The phase selection block with reconfiguration switches introduces a static phase rotation function. Each slice operates as a 2-bit VM, which has output phases of 0°, 90°, 180° or 270°. By combining multiple slices in a binary weighting scheme, higher number of bits in the VM constellation is accomplished (see Fig. 2). The TIA sums up the BB current from all VM slices at I_{TIA} and Q_{TIA}, and is converted to voltage output by feedback resistor R_{FB}. This combined output voltage in BB can be expressed as $V(m,n,o,p) = I + jQ$

$$\frac{4\sqrt{2}}{\pi\ M}\tilde{x}(t)gmR_{FB}\left((Ar_{\sum} + jAi_{\sum})e^{-j\omega_{bb}t}\right)\sum_{m=1}^{4}\sum_{n=1}^{4}\sum_{o=1}^{4}\sum_{p=1}^{4}$$
$$\left(8\ e^{j(m-1)\frac{\pi}{2}} + 4\ e^{j(n-1)\frac{\pi}{2}} + 2\ e^{j(o-1)\frac{\pi}{2}} + 1\ e^{j(p-1)\frac{\pi}{2}}\right) \tag{3}$$

where m, n, o, and p are selecting the phase of binary weighted slices. Equation (3) shows that all the weights are always used in each VM constellation point. All VM constellation points are generated by a combination of binary weighted slices with different phases. Equation (3) also shows that each slice in IF-RX provides the 90° combining of $V_{Ar\sum}$ and $V_{Ai\sum}$ with additional weights for combining/cancellation. For complex weighted, $V_{C\sum}$ summed input from the mmWave subarray, as shown in Fig. 1(b). The Castersian combining function of the IF-RX chip is not required. In that case, the IF-RX chip can be used with input $V_{Ar\sum}$ alone. By terminating $V_{Ai\sum}$, $Ai_{\sum}$ in (3) will be zero and IF-RX will only operate as VM for signal combining of mmWave subarrays to improve SNR and/or IBIC. The IF-RX chip processes $V_{Ar\sum}$ and $V_{Ai\sum}$ input signals, e.g., when it would be integrated with [23], both inputs are needed. For routing simplicity, we used the architecture of Fig. 1(b) here to demonstrate and characterize IBIC. Hence we only need one input.

B. IF-RX Circuit Design

The amplitude and phase constellation points of the VM depend on the number of slices. For M slices, the constellation consists of $M+1$ by $M+1$ points and contains $3M-1$ amplitude points on the largest circle that can be drawn inside the boundaries of the constellation. The implementation of the IF-RX is realized by dividing the input into 15 binary weighted, parallel slices where each slice acts as an independent vector component in the VM. The transistor-level implementation of a single slice is shown in Fig. 3. Each slice consists of a differential transconductor (gm), a double-balanced quadrature passive mixer for each differential $V_{Ar\sum}$ and $V_{Ai\sum}$ inputs and phase selection block at BB that adds current contributions of slices at the virtual ground node of the TIA. The static switch configuration is designed such that the current from each transcondutor always contributes to some output [18]. The TIA provides both BB *I-V* conversion and baseband low-pass filtering. An external reference clock at twice the local oscillator (LO) frequency is used to generate the four-phases 25% duty cycle clock by an on-chip current-mode logic divider and AND gate logic. The resulting clock is distributed across the chip to drive the mixer switches. The four-phase 25% duty cycle current mixer converts the IF transconductor current into zero-IF performs the Cartesian combining for $V_{Ar\sum}$ and $V_{Ai\sum}$ signals, and provides the differential I/Q signals. The phase selection block at BB rotates the I/Q signals by 0°, 90°, 180° or 270° depending on the phase constellation point.

C. Transconductor Stage

Two inverters serve as a pseudo-differential transconductor pair (gm) acting as LNTA and provide the input matching at the IF port (see center part of Fig. 3). In the inverter, both nMOS and pMOS contribute to the total transconductance and resistive feedback RF provides low NF and low impedance match due to the Miller effect [24]. The gm stage is DC-coupled with mixer switches to avoid the large ac-coupling capacitor in each slice. To avoid the dc operating point mismatch, a common-mode feedback (CMFB) stage is added to each differential pair and controlled independently through the current DAC. The pMOS transistors M_3 and M_5 are controlled by CMFB, and they feed the current at the output node of the gm stage depending on the common mode and bias input and output of the gm stage. Single slice gm stage devices use 7-u/40-nm transistors, including a feedback transistor with 3.5-kΩ feedback resistor R_F. The single slice provides a total gm of 8 mS. Each slice provides an input impedance of 800 Ω. By combining 15 parallel slices, the input impedance is $\approx$ 50 Ω.

D. Quadrature Downconversion

The Cartesian combining of the inputs $V_{Ar\sum}$ and $V_{Ai\sum}$ and the downconversion is realized with double-balanced quadrature passive mixer as shown in Fig. 3(a). The mixer consumes no static power and has a theoretical minimum conversion loss of 0.9 dB for 25% duty cycle with an additional 0.5-dB loss of Cartesian combining. The gate terminals (LO_{bias}),

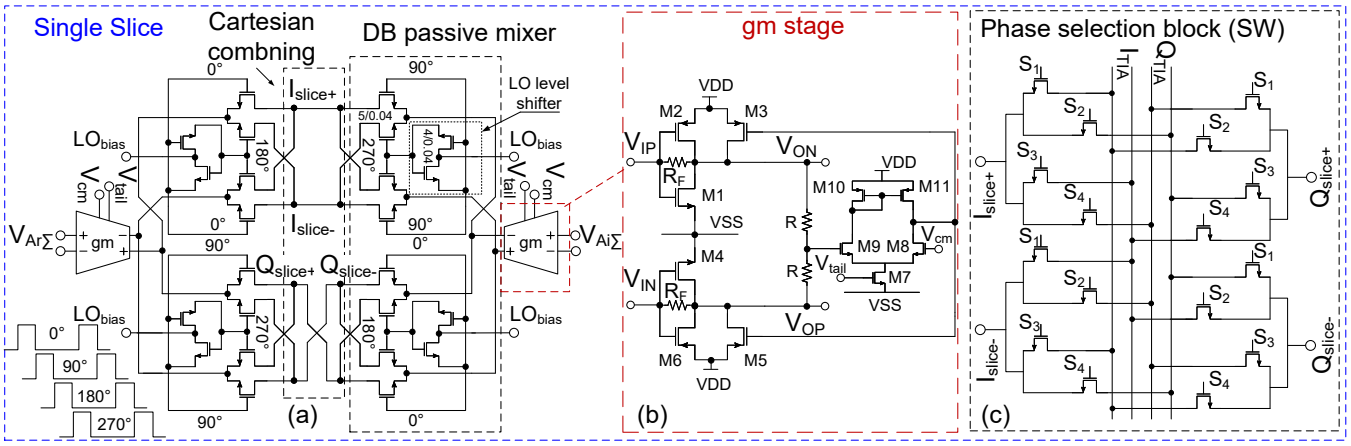

Fig. 3. Implementation details of a slice of the IF-RX shown in Fig. 2: (a) Cartesian combining with gm-block and passive mixer, (b) gm/transconductor stage, and (c) phase selection block (SW).

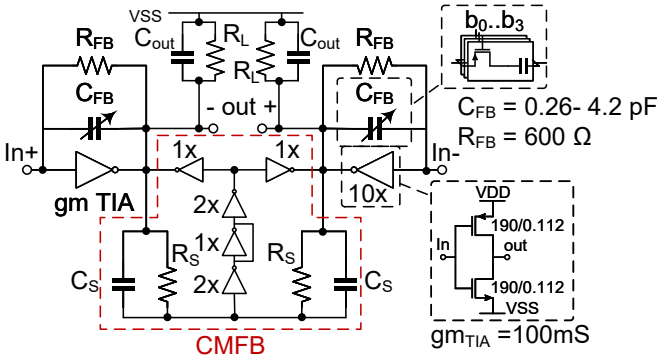

Fig. 4. Inverter-based baseband TIA stage (see also Fig. 2) with CMFB.

sources (biased from the gm side), and drains (biased from BB transimpedance amplifier (BB-TIA) side) of the mixer switches are biased to half of the supply and shift the DC-level of the LO locally to fully switch ON and OFF the mixer switches [Fig. 3(a)]. The I/Q signals generated in the mixer pair are further processed by the phase selection block. The switches are driven by static control signals and allow to pick one of the four mixer phases, which effectively rotate the phase by $0°$, $90°$, $180°$ or $270°$ [Fig. 3(c)].

E. BB-TIA Circuit

The inverter-based BB-TIA is implemented as in Fig. 4 to provide a better trade-off between power and noise performance compared to a single-stage Op-amp-based BB-TIA [26]. The BB-TIA is self-biased to approximately half of the VDD and has common mode feedback (CMFB) at the output to reduce the common-mode gain and even-order distortion. The TIA bandwidth depends on the R_{FB}, C_{FB}, input node capacitance, and output node load impedance. The pole frequency of the TIA voltage transfer function is $\omega_o = (C_{FB} + C_{out})(R_{FB}||R_{out}||R_L)$. For a fully integrated system, TIAs would typically directly drive an ADC or a buffer before the ADC. In our measurements, the TIA directly drives single-ended R_L = 50 Ω and C_{out} = 4 pF. The core of the TIA consists of two inverters, which each of them drives a single-ended 50 Ω load. High gm_{TIA} = 100 mS is used in the TIA stage, increasing the TIA´s current consumption. Low load impedance reduces the gain of the TIA but extends the bandwidth.

IV. Interference Rejection of Wideband Signals

A. Interference Rejection

Interference rejection of narrowband signals can be done by summing two signals with opposite phase. It has been applied for many purposes including reduction of non-linear distortion [27], to avoid LNA saturation in in-band full duplex transceivers [28], and also for spatial filtering [16]–[19], [29]. However, achieving sufficient amplitude and phase accuracy for cancellation purposes in circuit solutions is challenging over a wide bandwidth. Decent rejection has been demonstrated only for a rather narrowband modulation. In the case of 5G NR having RF bandwidths of several hundreds of MHz, this will become a major issue for any broadband cancellation scheme. Furthermore, even small time delays in a radio channel and differences in circuit realizations will impact the cancellation bandwidth (BW_{Canc}).

In case of beam-steered mmWave subarrays, the wideband rejection brings in one more challenge when two subarrays are receiving from different directions while still interfering with each other through sidelobes or even inside the main lobe. Then, the canceller [IF-RX C1 or IF-RX C2 in Fig. 1(b)] needs weights tuned to the interfering signal direction. Thus, the cancellation weights in IF-RX VM can differ from those in the mmWave subarrays. Hence, a calibration method for finding the most appropriate coefficients for the IBIC is needed.

B. Aspects of Wideband Rejection

Consider the simplified OTA model of the proposed architecture for IBIC in Fig. 5 to illustrate the limitations of the wideband interference rejection. The interference observed in A1 from TX2 is simulated by placing TX2 at an arbitrary angle from subarrays A1 and A2. In the model, phase shifts provided by A1, A2, IF-RX1, and IF-RX2 are modeled as mmWave and IF frequency-flat phase shifters and frequency downconverters,

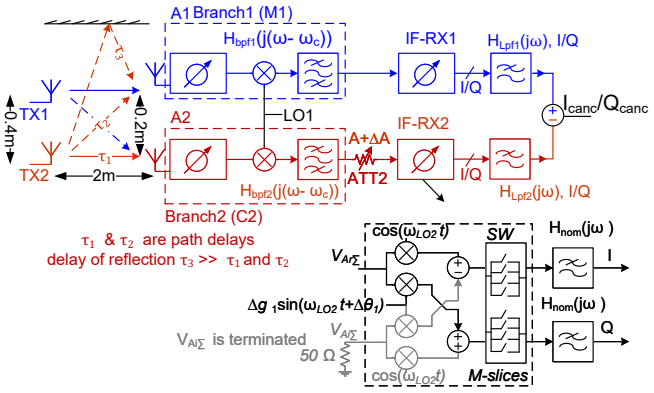

Fig. 5. Simplified OTA IBIC model of the proposed architecture.

with I/Q errors embedded in the IF-RX downconversion. The ATT is a part of the system to adjust the amplitude matching for interference cancellation. The IF bandpass filters $H_{bpf1,2}(j(\omega - \omega_c)$, each of them has a cutoff frequency of 2-4 GHz, is modeled by combining second-order high- and low-pass filter responses, and each BB filter $H_{Lpf1,2}(j\omega)$ has a second-order low-pass filter response. The limitations of the wideband rejection are separated into two categories: 1) branch mismatch errors and 2) OTA channel effects. The branch mismatch effects include circuit nonidealities and matching of components between branches. The OTA channel effects include delays between the different paths in the radio channel, potential multipath reflections in the radio channel, and variation in the received signal over the wide bandwidth due to the direction of an interferer.

1) Branch Mismatch Error Effects: The BW_{Canc} and the level of interference rejection depend on matching between the two branches and I/Q mismatch. The two branches may have differences, for example, in filter quality factors (Q_f), cutoff frequencies of the filters, the ripple in the filter responses, I/Q variation in IF-RX chips, and standing waves in circuits. When these two branches are combined to perform rejection, the resulting spectrum is evidently frequency-selective. To illustrate these effects, the OTA IBIC model was simulated without radio channel delays but with mismatch parameters added. The default mismatch parameters are selected for a maximum 30-dB rejection, which is limited by VM resolution at I_{Canc} and Q_{Canc} nodes. The following mismatch parameters are used: 1% mismatch between Q_f and cutoff frequencies of IF filters $H_{BPF1,2}(j(\omega - \omega_c))$, 2% error in attenuators, 1% cutoff frequency error between $H_{LPF1,2}(j\omega)$ filters and 4% I/Q mismatch error between the IF-RX chips. The simulated BB response of the OTA IBIC model with mismatch parameters is shown in Fig. 6(a). The rejection response at the I_{Canc} and Q_{Canc} nodes in BB results in >30 dB of notch at I_{Canc} (solid red curve) and ≈28 dB at Q_{Canc} (dashed red curve) node shown in Fig. 6(b) (red curves only) with zero delay difference between branches 1 and 2. It shows very wideband rejection for a minimum of 20-dB rejection. After combining in BB, $I_{Canc} + jQ_{Canc}$ results in further reduction of interference rejection due to I/Q mismatches which results in frequency selective rejection as shown in Fig. 6(c) (red curve). The

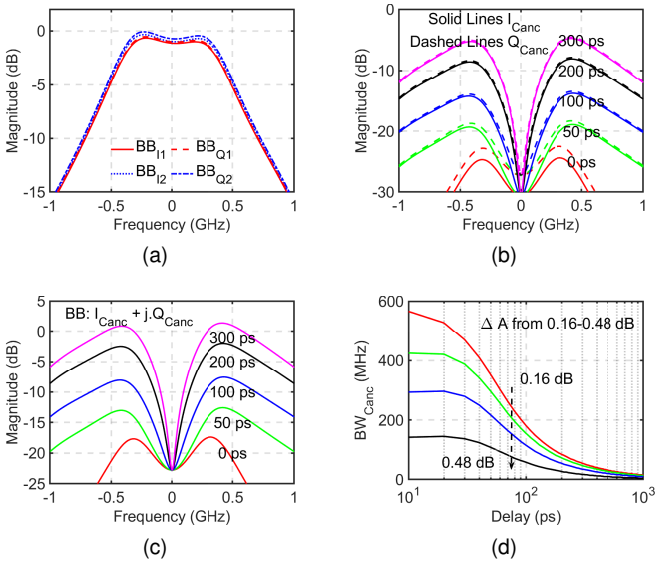

Fig. 6. (a) Simulated BB responses of branches 1 and 2 with mismatch parameters. (b) I_{Canc} and Q_{Canc} with and without delay difference ($\tau_1 - \tau_2$) between branches (c) combining I_{Canc} + jQ_{Canc} (d) BW_{Canc} for minimum 20-dB of cancellation with different error in ΔA.

model simulations show that the interference rejection and its BW_{Canc} are sensitive to the I/Q and amplitude mismatch errors. Fig. 6(d) shows the cancellation BW_{Canc} for 20-dB rejection with different amplitude mismatch errors. It shows that when the OTA channel delays are zero, the maximum cancellation BW_{Canc} is constrained by mismatch errors, but >400 MHz would be feasible for 0.25 dB.

2) OTA Channel Delay Effects: In the OTA channel time delays, τ_1 and τ_2 are slightly different due to the angle and location of the interferer (TX2) with respect to the physical positions of the receiver elements and arrays. It means that the cancellation and main paths are summed together with a delay difference. As indicated in Fig. 6(b) and (c), the BW_{Canc} will be further narrowed as compared to frequency-flat phase shifter due to the fact that the slopes of the phase responses are different. When branch mismatch errors are the worst, the cancellation BW_{Canc} will be more sensitive to small delays. It imposes a limit on how much delay the system can tolerate for a particular BW_{Canc}. Third, multiple propagation paths may exist even in the line-of-sight (LOS) channels, and they usually have lower amplitude but much longer delay (τ_3) than the main propagation paths (τ_1 and τ_2). Even small reflections will cause ripples in signals seen in the main and cancellation paths, limiting the cancellation further. In a simple two-path model, the ripple frequency depends on the delay in the reflection (this effect is further discussed in Section VI).

C. Power and EVM based Calibration Method

In order to cancel the interference, the cancellation coefficients must be first found. This can be done in many ways in the digital and analog domains depending on the hardware implementation. For example, Cao and Zhou [30] and El Sayed et al. [31] implemented analog circuitry using least mean square (LMS) method to train the cancellation, while

Nagulu et al. [32] optimized gains and delays using the digital iterative feedback loop algorithm. In [21], the cancellation coefficients were found by using exhaustive search. In this article, the main objective is to reach cancellation performance over the entire signal bandwidth. To this end, we apply power-based and EVM-based calibration method to calibrate the VMs for good cancellation performance. Hence, the calibration method has two steps. In the first part the aim is to find the phase shifter value that minimizes the power of the sum signal containing the interference. The second part is simple fine-tuning using EVM measurements, mainly to verify the cancellation performance.

Let the signal observed at the A1 output be $s_1 = x_1 + a_{12}e^{j\phi_{12}}x_2$ and signal at A2 output $s_2 = a_{21}e^{j\phi_{21}}x_1 + x_2$, where x_1 and x_2 are the received signals transmitted from the TX1 and TX2, respectively, and a_{nm} and ϕ_{nm} are the relative amplitude and phase of signal n observed at subarray m, respectively. After cancellation, the aim is to see only x_1 in A1 output and only x_2 at A2 output. Let us first calibrate the cancellation to cancel x_2 from the A1 output. After the RF beamforming, it is expected that $a_{12} < 1$ and $a_{21} < 1$, i.e., the signal-to-interference ratio (SIR) is positive in decibels at both array outputs. Let us denote the VM phase value applied for the cross-coupled path from A2 to A1 as ϕ_{ps}. By summing the phase-shifted version of the A2 output to the A1 output, we get

$$\begin{aligned} s_{1,\phi_{ps}} &= s_1 + a_{12}e^{j\phi_{ps}}s_2 \\ &= \underbrace{(1 + a_{12}a_{21}e^{j(\phi_{21}+\phi_{ps})})}_{\approx 1, a_{12}a_{21}<<1} x_1 + (a_{12}e^{j\phi_{12}} + a_{12}e^{j\phi_{ps}})x_2 \\ &\approx x_1 + a_{12}(e^{j\phi_{12}} + e^{j\phi_{ps}})x_2 \\ &= x_1 + a_{12}e^{j\phi_{12}}(1 + e^{j(\phi_{ps}-\phi_{12})})x_2 \\ &= x_1 + 2a_{12}e^{j\frac{1}{2}(\phi_{ps}+\phi_{12})}\cos(\frac{1}{2}(\phi_{ps} - \phi_{12}))x_2. \end{aligned} \quad (4)$$

Now, assuming that x_1 and x_2 are independent signals, the power $P_{1,\phi_{ps}}$ of the sum signal at the A1 output with phase shifter value ϕ_{ps} can be written as

$$\begin{aligned} P_{1,\phi_{ps}} &= P_1 + 4a_{12}^2(\cos(\frac{1}{2}(\phi_{ps} - \phi_{12}))^2 P_2 \\ &= P_1 + 2a_{12}^2(1 + \cos(\phi_{ps} - \phi_{12}))P_2. \end{aligned} \quad (5)$$

The result has maximum ($= P_1 + 4a_{12}^2P_2$) when $\phi_{ps} = \phi_{12}$ and minimum ($= P_1$) when $\phi_{ps} - \phi_{12} = 180^\circ$ which gives the cancellation based on (4). Based on (5), finding the cancellation phase turns into a problem of finding the initial phase of the cosine in (5) with minimum number of used phase shifter values ϕ_{ps}. The phase shift can be measured by sampling it four times over the period of the cosine. In general, this means that we need to measure with four different phase shifter values to get the desired cancellation coefficient. Hence, we measure with $\phi_{ps} = \{0^\circ, 90^\circ, 180^\circ, 270^\circ\}$ and note the points as $\{P_{1,0}, P_{1,90}, P_{1,180}, P_{1,270}\}$. Based on these, the real and imaginary parts whose relation describes the required phase shift of the cancellation path can be derived as

$$\mathrm{Im}(e^{j\phi_{canc}}) = \frac{1}{2}(P_{1,180} - P_{1,0}) \quad (6)$$

$$\mathrm{Re}(e^{j\phi_{canc}}) = \frac{1}{2}(P_{1,270} - P_{1,90}). \quad (7)$$

The phase that minimize (5) can be calculated using $\arctan(\mathrm{Im}/\mathrm{Re})$. Note that the correct phase can also be realized by applying the real and imaginary values given in (6)–(7) directly to the VM after normalizing the phasor absolute value to one. More points can also be measured to improve the estimation accuracy. A similar analysis can be made for cancelling A1 output from A2 output. Note that the described process aims first for calculating the phase of the cancellation coefficient. Hence, even if the applied amplitude coefficient a_{12} would not be accurate, the sum signal observed over the phase shifter states has still the same minimum. Hence, once the minimum is found, the system can re-tune the amplitude to improve the performance. Initial guess of a_{12} can be estimated, for example, based on SIR (linear scale) observed at A1 output without cancellation as $a_{12} = 1/\mathrm{SIR}_1$. This can be derived, for example, based on received EVM or SNR, or even based on the known calibrated beam shape relation with respect to the steering directions.

Choosing a phase value to minimize the power of the interference results in zero-forcing coefficients. However, this does not necessarily mean that the signal quality is maximized due to the fact that the interference nulling may have a slight impact also on the useful signal. This is the case especially when the interference is rather strong. The second stage of the calibration method takes a fixed amount of EVM measurements with different phase shifter values from both sides of the estimated power minimum to tune the calibrated coefficient for minimizing the EVM. The two-stage calibration method is demonstrated by OTA measurements in Section VI-B1.

V. IF-RX Measurements

A. General Setup

The IF-RX was realized on-chip in 45-nm PDSOI CMOS process. The chip has an active area of 0.28 mm^2, including clock generation. The circuit consumes 104 mW of power from a 1-V supply and 10 mW from a second 1.5-V supply for buffers to drive static switches. Fig. 7(a) shows a chip photograph with the placement of the various receiver blocks with their power consumption. The IF-RX chip measurements are performed using external 1:2 impedance baluns at the RF, BB, and LO ports of the printed circuit board (PCB) shown in Fig. 7(b).

Conversion gain and linearity measurements were performed using a four-port vector network analyzer (VNA). An external splitter followed by passive balun on PCB is used to drive differential $\mathrm{V}_{\mathrm{Ar}\sum}$ and $\mathrm{V}_{\mathrm{Ai}\sum}$ RF inputs. The BB I and Q outputs are measured through passive baluns on PCB as shown in Fig. 8. The external passive balun (MTX2-73+), used at the RF and LO ports has 2–7-GHz bandwidth. Below 2.5 GHz, the external balun restricts the bandwidth of the wideband RF response in measurements. The RF frequency response of IF-RX chip is measured at 50-MHz offset across LO frequencies from 1 to 4 GHz. The IF-RX chip has a maximum conversion gain of 15 dB at 2.5 GHz shown in 9(a). Fig. 9(b) shows the

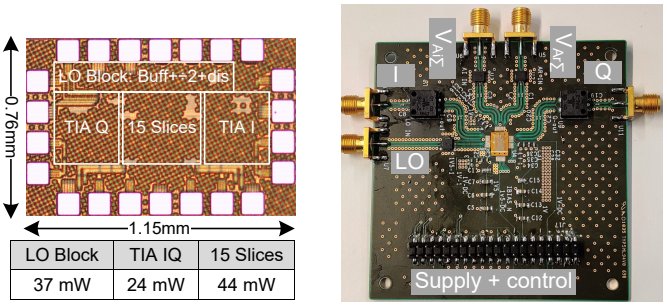

LO Block	TIA IQ	15 Slices
37 mW	24 mW	44 mW

(a) (b)

Fig. 7. (a) Chip photograph of IF-RX with power consumption of each block and (b) PCB photograph.

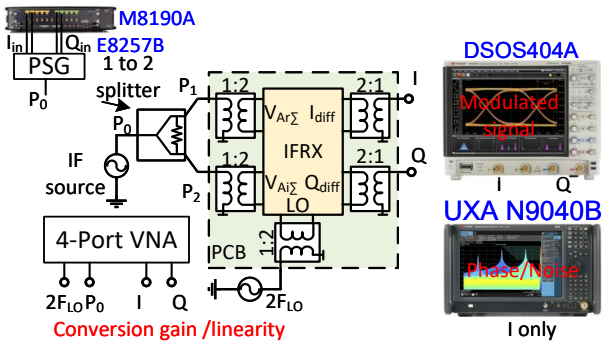

Fig. 8. IF-RX chip measurement setup.

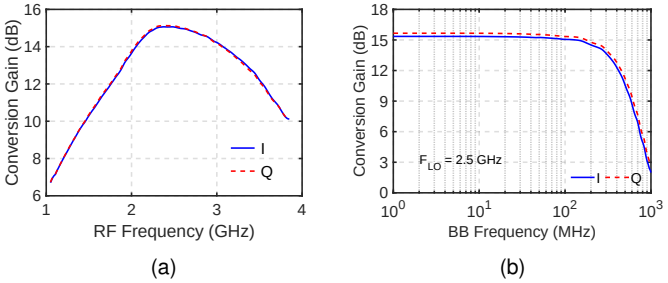

(a) (b)

Fig. 9. (a) Measured RF frequency response at fixed BB = 50 MHz (b) BB frequency response at F_{LO} = 2.5 GHz.

measured BB response at a fixed LO frequency of 2.5 GHz. A conversion gain of 15 dB and a -3-dB bandwidth of 400 MHz are measured at both I and Q outputs.

The setup described in Fig. 8 is used to measure NF with a UXA N9040B signal analyzer. Only the $V_{Ar\Sigma}$ input is used and $V_{Ai\Sigma}$ is terminated. At a fixed 50-MHz BB, a double sideband NF ($NF_{DSB,eq}$) of 5.5-8.5 dB is measured across LO frequency, and 5.5-9 dB is measured for variable BB at fixed RF band, as shown in Fig. 10(a) and (b), respectively. The measurement shows a minimum of 5.5-dB NF_{DSB}. Because the IF-RX chip is placed after the mmWave module with LNA and beamforming in the system, its noise contribution to overall system noise is minimal. The measured third-order intercept point (IIP3) both for in-band and out-of-band (OoB) is shown in Fig. 11(a). For the in-band IIP3 measurements, two tones f_1 and f_2 are at Δf - 2.5 MHz and Δf + 2.5 MHz, respectively. Note that Δf represents the offset from the LO frequency (f_{LO}) and f_{LO} =

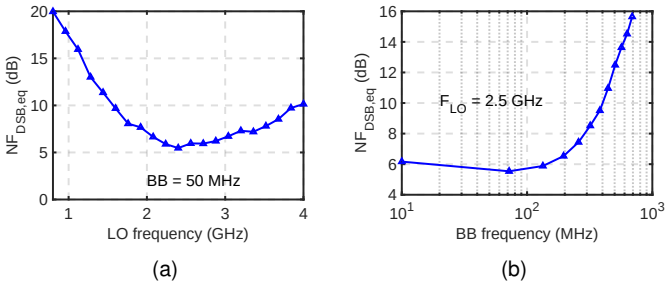

(a) (b)

Fig. 10. (a) Measured $NF_{DSB,eq}$ at 50 MHz BB and (b) measured $NF_{DSB,eq}$ at 2.5-GHz LO.

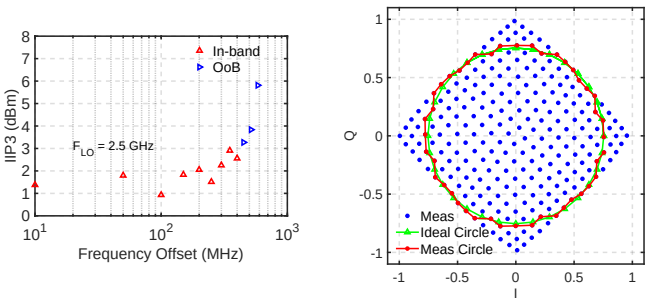

(a) (b)

Fig. 11. (a) Measured in-band and OoB IIP3 at 2.5 GHz (b) phase constellation of constant Gm-vector modulator measured at 2.5-GHz LO.

2.5 GHz in the measurement. IIP3 is more than +1 dBm for all Δf within the measured TIA bandwidth of 400 MHz. For the OoB IIP3 measurement, two tones f_1 and f_2 are at Δf and $2\Delta f$ - 50 MHz such that the IM3 products always falls at 50 MHz. OoB linearity follows the inverse of the BB frequency response as shown in Fig. 11(a).

B. VM Measurement

Relative amplitudes and phase shifts of all the possible VM settings are measured with the UXA N9040B IQ analyzer option using the setup shown in Fig. 8. The UXA splits the measured signal into I and Q vectors. This measurement uses a single RF tone with a 50-MHz offset from the LO at 2.5 GHz. By taking the first measurement as a reference, all the control words of the VM were swept and the resulting I/Q vector constellations are shown in Fig. 11(b). The rms phase error of the VM is 1.48°, the rms amplitude error is 0.33 dB, and the largest circle in the constellation has rms 8° of resolution. The outer circle in Fig. 11(b) will be used both for rejection and calibration methods.

C. Modulated Measurements, Image Rejection, and EVM

Signal quality and I/Q image rejection were characterized with EVM measurements. The 5G NR 50, 100, and 200 MHz [2 x 100 MHz per component carrier (CC)] signals with cyclic prefix OFDM (CP-OFDM) FR2 were used in the measurements. A M8190A arbitrary waveform generator (ARB) by Keysight is used as a source to generate the wideband signal, and a E8257B vector signal generator (PSG) up-converts the signal to 2.55-GHz IF frequency (Fig. 8). The DSOS404A oscilloscope combines the IF-RX chip I/Q

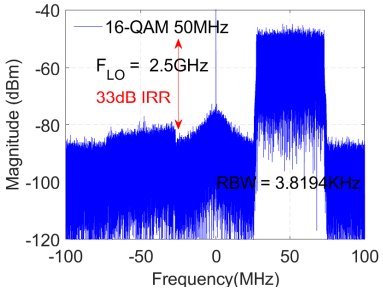

Fig. 12. Measured IRR: Input to $V_{Ar\sum}$ and $V_{Ai\sum}$ terminated.

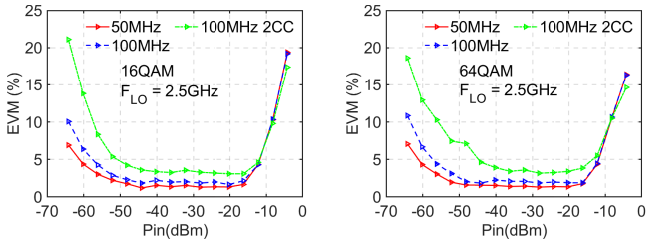

Fig. 13. (a) Measured EVM: (a) 16 QAM signal (b) 64 QAM signal (single input $V_{Ar\sum}$ is used and $V_{Ai\sum}$ is terminated.)

output at BB. Leakage signal suppression was measured only feeding input $V_{Ar\sum}$ while $V_{Ai\sum}$ was terminated. A 16 QAM 50-MHz modulated signal is generated for the test, and after de-embedding the fixture losses, the power level at the IF-RX chip input is -25 dBm. Fig. 12 shows 33-dB suppression of the leakage signal.

Conductive EVM measurements were performed for a single-input case using 16 QAM and 64 QAM modulations. For 50- and 100-MHz signals, the RF is set to a frequency offset of 60 MHz from the LO, and for 2 x 100 MHz CC signal, the LO is in the middle of the CCs. The measured EVM curves as a function of the input power are shown in Fig. 13, illustrating that the IF-RX chip has more than 50 dB of dynamic range. The best achieved EVM is 1.4% for 50 MHz, 2 to 2.2% for 100 MHz, and 3%–4% for 2 x 100 MHz wide signals.

VI. Over-the-Air Measurements

In this work, the IBIC scheme is introduced to provide interfering signal cancellation in the analog domain. This will cause a decent reduction in the required ADC dynamic range and reduces the need of cancellation in the digital domain. The OTA measurements are performed to show the effectiveness of the spatial filtering with the IBIC scheme using EVM and beam pattern as in [21], [33]. IBIC was initially demonstrated using a continuous-wave (CW) signal in [21]. In this section, the IBIC measurements were performed for wideband signals using the setup as shown in Fig. 14. Wideband cancellation includes the frequency dependence not visible in many earlier state-of-the-art papers, in which the signal bandwidth 50 MHz or below [12], [13], [15]–[19]. The measured IBIC results are compared with the OTA theoretical IBIC model for wideband signal described in Section IV-B. Focus is on the non-idealities of the system and delays in the radio channel that limit the cancellation $\mathrm{BW_{Canc}}$.

A. mmWave OTA Setup and Link Parameters

The modulated signal OTA measurements were performed using a setup shown in Fig. 14. The measurements used two M8190A ARBs, I/Q up-converters, conventional PAs (CA2630-141), and horn antennas (A-info LB-28-15) on the transmitter side. A DSOS404A oscilloscope was used on the receiver side to measure the I/Q signal at BB. The 28-GHz front end of [34] has two 16 x 4-element subarrays (A1 and A2) with 16 electrically controllable phase shifters, one for each 2 x 2 hard-wired antenna subarray. The common path of each subarray has a 31-dB range 5-bit digitally controlled attenuator. Physically, A1 and A2 are horizontally aligned on top of each other, and they provide an IF output from 3 to 4 GHz. The outputs are combined at BB using the IF-RX chip shown in Fig.14. A single input $V_{Ar\sum}$ of the IF-RX chip is used, and the other input is terminated to 50 Ω because the mmWave subarray provides a complex weighted IF output.

To evaluate the system gain and NF parameters, a 2-meter OTA link with subarray A1 and IF-RX1 on and subarray A2 and IF-RX2 off is analyzed. At 28-GHz, the signal has 61 dB of loss for a 1-meter distance in the OTA channel. For effective isotropic radiated power (EIRP) of +17 dBm at the transmitter antenna, the input at the receiver antenna array is -50 dBm. After combining at mmWave before the mmWave attenuator, the front end subarray has a typical gain of 35 dB, including a 12-dB array gain. The downconversion from 3.5-GHz IF to BB has a 2-dB of loss, including cable, PCB, and BB combiner losses and gain of the IF-RX. The attenuator in the signal path is set from 17 to 20 dB to adjust for optimum performance of the 28-GHz front end, resulting in 14-17-dB of gain from antenna array to BB output I port having NF of 9 dB. In case of modulated measurements, the system has an additional 3-dB I/Q combining gain in BB.

In Fig. 14, the signal (blue) is at 0° direction, and the interference (red) is at -10°. The measurements were carried out with 5G NR 16 QAM and 64 QAM OFDM signals, and minimal EVM requirements for demodulating the signals are 12.5% and 8%, respectively [35]. The signal and interference are transmitted at 27.9 GHz. The EIRP of the transmitted signal is +17 dBm, and the interference EIRP is adjusted $\approx$10 dB stronger than the signal. On the receiver side, A1 is steered to 0° and A2 to -10° to receive both of them. The A1 and A2 mmWave subarrays utilize an in-house developed beamforming calibration scheme [36], which equalizes the main beam gain at different angles and reduces the SLLs below 13 dB for specific steering angles. The 3.5-GHz IF output is downconverted to BB with a center frequency of 60 MHz for 50- and 100-MHz wide single-carrier (SC) OFDM signals and zero offset for multicarrier signals. The BB I/Q outputs were combined using a DSOS404A oscilloscope.

B. OTA Modulated Measurements

In OTA modulated measurements, we will demonstrate: 1) IBIC after calibration of IBIC VM-coefficients; 2) OTA IBIC

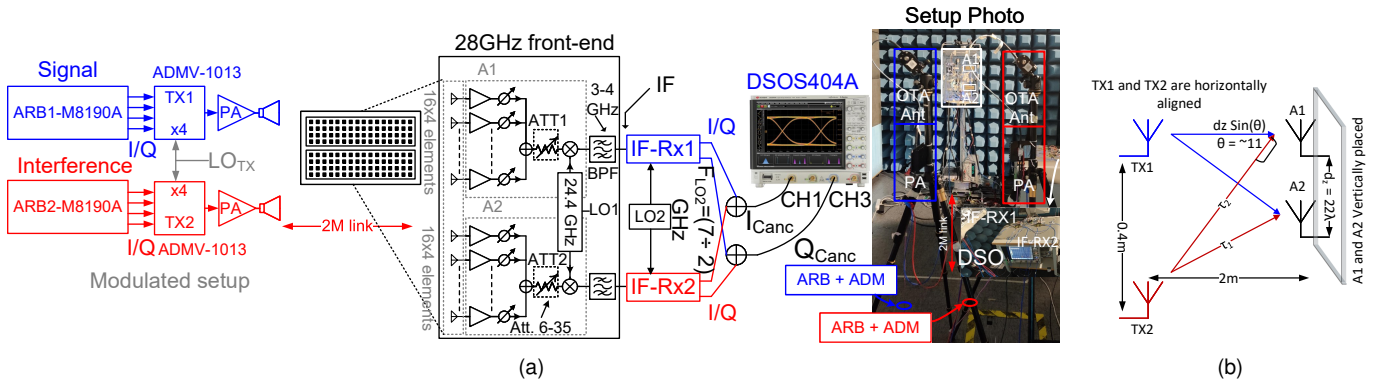

Fig. 14. OTA modulated measurement setup and lab photograph of the setup in an anechoic chamber (b) placement of transmitters and A1 and A2 for calculating the radio channel delay difference $(\tau_2 - \tau_1)$ between A1 and A2 receiver.

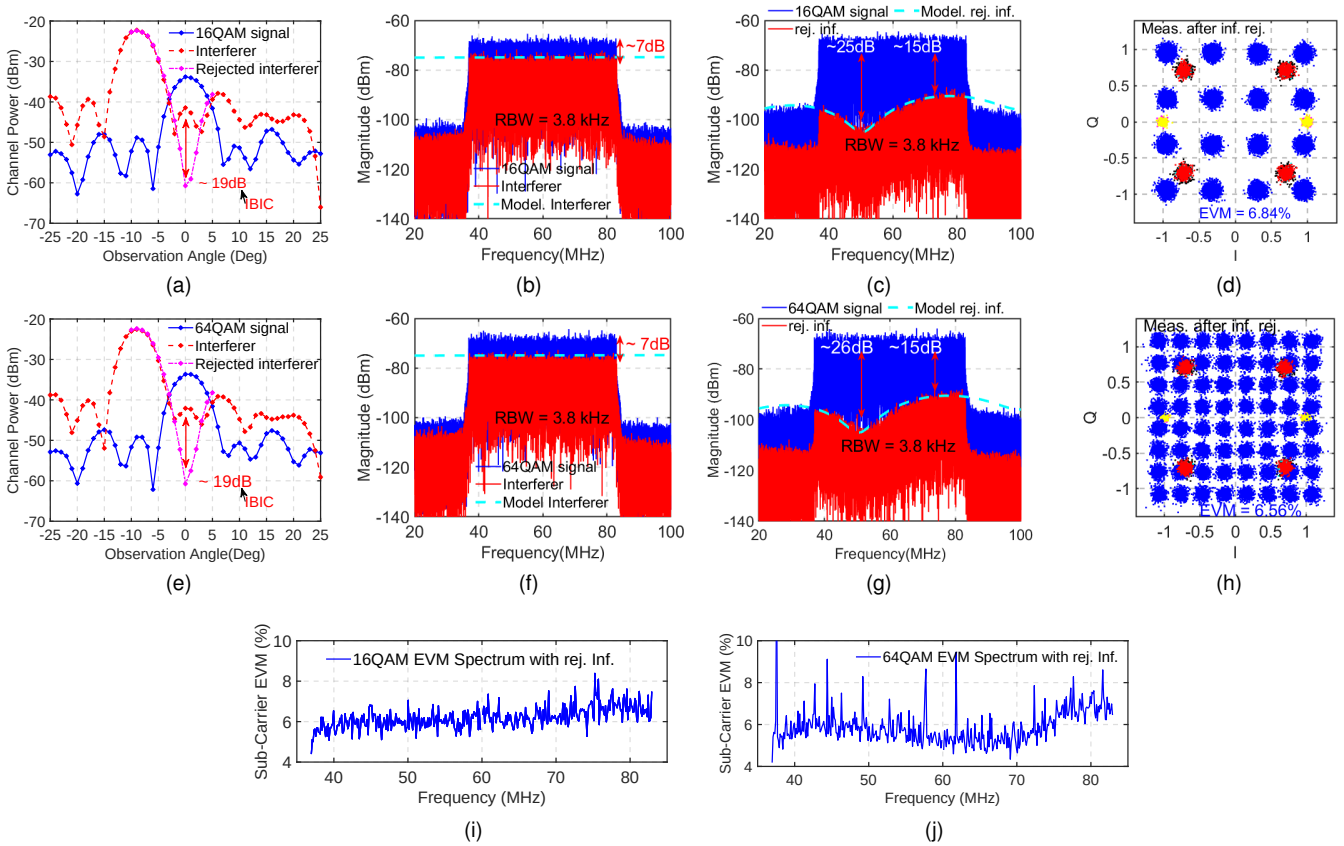

Fig. 15. (a) Signal and interferer beam and interferer rejected at 0° (b) measured 16 QAM 50-MHz signal and interference at the output IF-RX1 (c) signal after interference rejection. In (b) and (c) measured spectrum before and after rejection are compared with OTA IBIC model (d) EVM with interference rejection (e) - (h) 64 QAM 50-MHz signal with interference rejection measurements. Spectral representation of rms EVM sub-carriers of 16 QAM (i) and 64 QAM (j) signals.

model validity and how we obtained branch mismatch and delay parameters to fit the model to measurements; and 3) wideband IBIC in a 5G NR carrier aggregation system.

1) Calibration of IBIC Coefficients : A 16 QAM 50-MHz modulated signal is used to demonstrate the calibration of complex cancellation coefficients. We first calibrated the amplitude matching between the main and cancellation paths. It requires information of the spatial filtering of the interferer by mmWave subarray. In this measurement, the interferer is $\approx$ 10 dB stronger than the signal, and its first sidelobe is in the main beam of the signal, as shown in Fig. 15(a). The interference and signal levels are measured at BB of the A1 receiver chain to verify spatial filtering by activating one TX at a time. During these measurements, the VM of the IF-RX1 and IF-RX2 chips is set at the outer circle and provide no phase rotation. The mmWave subarray spatially filters the 10-dB stronger interferer, and the received interference SLL is 7 dB below the signal in the direction of 0° [red curve in Fig. 15(a)]. After spatial filtering, the signal and interference spectrums can be seen in Fig. 15(b), showing the 7-dB SINR that corresponds to 34% EVM. After this measurement, the amplitudes are matched between A1 and A2 by using the

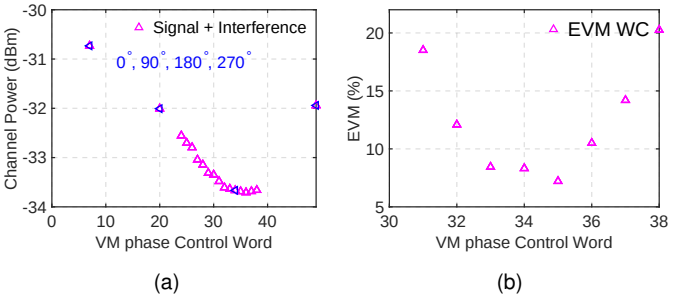

Fig. 16. Calibrating the phase of the cancellation coefficients using 16 QAM (a) phase1: interference power level after rejection is used to find the best cancellation coefficients. The lowest values indicate the lowest interference level (b) phase2: fine-tuning of the control word is done by minimizing the EVM when the interferer is present.

attenuators in the mmWave subarray modules. The attenuation in the cancellation path depends on the difference between the main beam and the SLL of the interferer and is adjusted accordingly. The measured beam pattern of the interferer in Fig. 15(a) (red curve) suggests that for amplitude matching, the difference between ATT1 and ATT2 is 18 dB.

In modulated measurements, the phase cancellation coefficient calibration method described in Section IV-C is performed in two phases and validated. Both TXs and RXs are turned on for calibration of the cancellation coefficients. A1 receives the signal with interference. In the measurements, attenuators in A1 and A2 are used to match the amplitude in the cancellation path, allowing cancellation to be done with the outer circle of the VM (better resolution). In the first phase, the channel power is measured at 0°, 90°, 180° and 270° phases by changing the VM quadrant (IF-RX2) phase controls, as shown in Fig. 16(a) (shown in blue markers). The fine-grained VM phase controls are then searched toward the lowest power level. The lowest power value in Fig. 16(a) indicates the lowest interference level, and the maximum value corresponds to the maximum interference level. Based on the signal plus interferer measurements in BB, the required cancellation phase can be approximated for minimizing the interference.

The estimated cancellation phase does not always correspond to the minimum EVM because the rejected interference also has a fraction of the signal. Therefore, the EVM is fine-tuned by re-calibration with N-points close to the cancellation phase in the second phase. Based on the channel power measurements as shown in Fig. 16(a) (magenta points), the calculated cancellation phase for optimized EVM is -72° according to (6) and (7), which corresponds to VM phase control word 35. Measurement results in Fig. 16(b) (magnified from 31 to 38) confirm that the channel power-based initial estimate is, in this case, also equal to the control word of the optimized EVM. The digital demodulation constellation after IBIC is shown in Fig. 15(d). The amplitude matching, phase finding, and fine-tuning of the EVM measurements were automatized and take 11 measurements to complete one iteration. Most of the time the best EVM is achieved in one iteration.

2) All Branch Mismatch Errors: The nonidealities in the measurements are estimated using the OTA IBIC model. The OTA IBIC model uses the same branch mismatch parameters values without delays given in Section IV-B, tuning ΔA, OTA delay between branches ($\tau_2 - \tau_1$), and cancellation frequency to match the model with measurements. The additional multipath reflection signal is added in the model to estimate the delay in the path of reflection (τ_3). The OTA IBIC model is matched with measurements in three steps: matching null by tuning ΔA and the cancellation frequency without OTA delays in the first step; and Then include delay difference between branches and multipath reflection delay and magnitude. The null matching provides the estimated I/Q imbalance; and the second and third steps model the rejection spectrum and BW_{Canc} by estimating OTA channel delays.

Fig. 15(b) shows the signal and the overlaying interferer without IBIC have both a flat frequency response over 50-MHz of signal bandwidth. In the OTA IBIC model, the interferer level is set to the measured level of interference before the rejection. Fig. 15(c) shows the measured signal and interference spectrum after rejection with the simulated rejection (light blue curve). The simulated response in 15(c) is a combination of all branch mismatch errors, including OTA channel delay between branches and multipath reflection components. It is achieved in three steps as described. The null matching is achieved by tuning the center frequency and ΔA difference to 4% without delay between branches. This results in 0.37 to 0.4 dB amplitude and up to 2° phase error. After combining in BB, this I/Q imbalance error corresponds to $\approx$ 0.9-dB amplitude and up to 6° phase error. This parameterization shows good agreement with the measured null depth of 25 dB shown in Fig. 15(b).

OTA channel delays are included in the simulated model to match with the measured spectrum after rejection. OTA channel delay difference ($\tau_2 - \tau_1$) depends on the spacing between the arrays and the angle of the interferer. The $\tau_2 - \tau_1$ value can be calculated using simple trigonometry for a LOS channel. In the testing configuration, the spacing between arrays is 22λ at the carrier frequency, and the interferer is at an angle of about $\approx$11 degrees, resulting in a $\approx$153 ps delay difference. The multipath reflection component is added to the OTA IBIC model, and the delay τ_3, the multipath reflection amplitude and cancellation frequency are tuned in the model to match the measured rejected interferer spectrum in Fig. 15(c). The resulting magnitude of the multipath component is 30 dB below the interferer, and τ_3 is $\approx$20 ns. The combined simulated effect in Fig. 15(c) (light blue) shows that the OTA IBIC model can be used to estimate the non-idealities in the system with good accuracy.

Fig. 15(c) shows the achieved cancellation BW_{Canc} above 20-dB rejection is 30 MHz and more than 50 MHz for 15-dB of rejection. The measured demodulated signal constellation after rejection is shown in Fig. 15(c). After rejection, 6.8% rms EVM is achieved. The interference rejection in terms of channel power can be quantified from the measured beam pattern of the interferer after rejection [see Fig. 15(a), magenta line], which shows 19-dB of rejection. At the rejection null, the SINR is mainly limited by the noise floor of the signal in

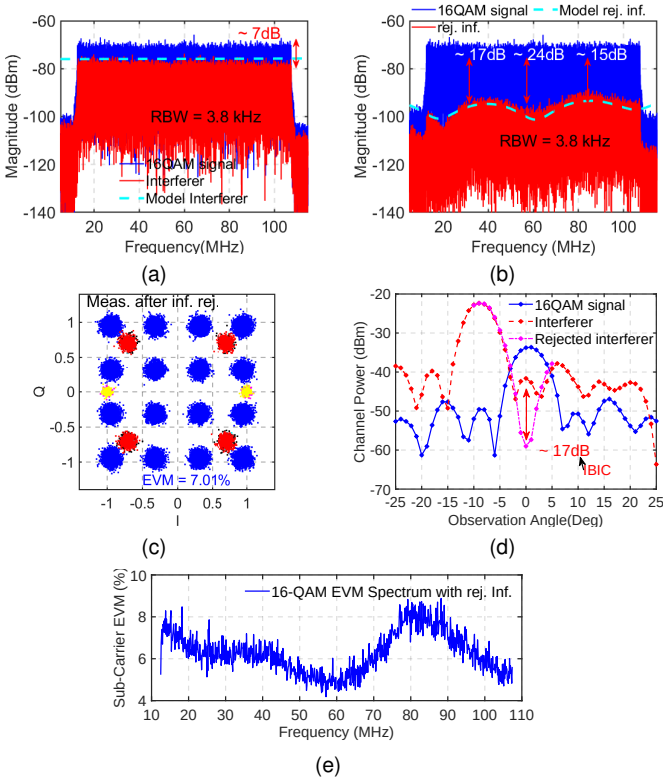

Fig. 17. (a) 16 QAM 100-MHz signal and interference at the output IF-RX1 (b) Interference rejection, in (a) and (b) measured spectrum before and after rejection are compared with the OTA IBIC model (c) constellation with interference rejection (d) signal and interferer beam with and without interference rejection (e) rms EVM spectrum of each sub-carrier.

this measurement, which results in SINR of 23 to 25 dB and rms EVM of 6.84%, which can be verified from the sub-carrier rms EVM spectrum, as shown in Fig. 15(i). The reliability of the calibration method and measurements is double-checked with 64 QAM signal, and the results are in Figs. 15(e)-(h) and (j) showing similar rejection performance.

3) Reflections at mmWave in the OTA Channel: Another set of interference rejection measurements were performed for a 100-MHz wide signal to evaluate the impacts of multipath components in the radio channel. Those are causing differences between the cancellation path and the interference path. These are frequency dependent and seen as ripples in the response, as shown in Fig. 17(b). This is verified with simulations by changing the cancellation frequency in the OTA IBIC model and keeping all the other parameters the same as described in previous OTA 50-MHz signal measurements. The simulated response can be seen in Fig.17(a) and (b). The OTA IBIC model with delayed multipath component (τ_3 = 20 ns) confirms the ≈50 MHz periodicity in the rejected spectrum due to multipath reflections in Fig. 17(b) and shows ≈ 15 dB of minimum rejection over 100-MHz bandwidth. Figs. 17(c) and (e) shows the corresponding demodulated signal constellation and EVM spectrum. Wideband rejection results in 7% rms EVM and achieved 17-dB rejection in terms of channel power when integrated over all sub-carriers (see Fig.17).

4) Wideband Rejection in Carrier Aggregated Systems: As relative bandwidth increases frequency dependence becomes

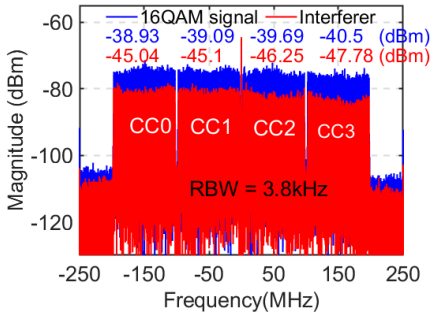

Fig. 18. (a) 16 QAM 4 x 100 MHz signal before cancellation with interference at the output IF-RX1.

even more prominent. In broadband systems, a single-tap analog canceller as shown above has fundamentally limited cancellation performance over the spectrum. One way to improve the rejection bandwidth is to divide the processing into multiple separate channels to equalize the frequency response and match the OTA channel delays in sub-bands. For example, in 5G NR, carrier aggregation schemes are used to divide the overall band into multiple CCs. To illustrate this mode of operation, a 4×100 MHz signal is used in the measurements to demonstrate multi-tap performance over several CCs in OTA cancellation. Fig. 18 shows the frequency spectrum of the signal and the interferer. From CC0 to CC3, the signal amplitude varies by 1.5 dB, and the interferer amplitude varies by 2.7 dB. It is because the IF-RX chip has a non-flat response around 3.5-GHz input and some additional in-band ripple in the IF BPF of the mmWave front end [34]. Under these constraints, single CC cancellation can be accomplished by matching amplitudes with attenuators in the mmWave front end and calibrate each CC separately in the cancellation process. It is shown for each CC separately in Fig. 19. For more than 15-dB of rejection needed for successful digital demodulation of each CC, the amplitudes for a particular CC are adjusted at a time. In that case, the amplitude matching error is between 0.8 to 1.1 dB, and the multipath reflections delay is between 17 to 20 ns. Figs. 19(a)-(d) show the measured rejection spectrum and simulated rejection response of each CC by matching the amplitude of single CC at a time. In the simulations, all the parameters were the same except the delay of the multipath reflections for each CC and matched the response by tuning cancellation frequency and delay of the multipath reflection to match each other. The achieved rms EVM for each CC after rejection is from 7.3 to 9.3% [Fig. 19(e)-(h)], and the rejection in terms of channel power is from 16 to 17 dB. Better performance would require four parallel cancellers one for each 100-MHz CC in this case.

C. Cancellation Performance Comparison

Comparing wideband cancellers for realistic OTA scenarios is never a straightforward task. As shown in this article, cancellation always has limited bandwidth, not only depending on the relative frequency or the cancellation technique but also on the radio channel and how the rejection has been tested. Many of the cancellation schemes referred to in this section *are working fine for the CW tone or low bandwidth*

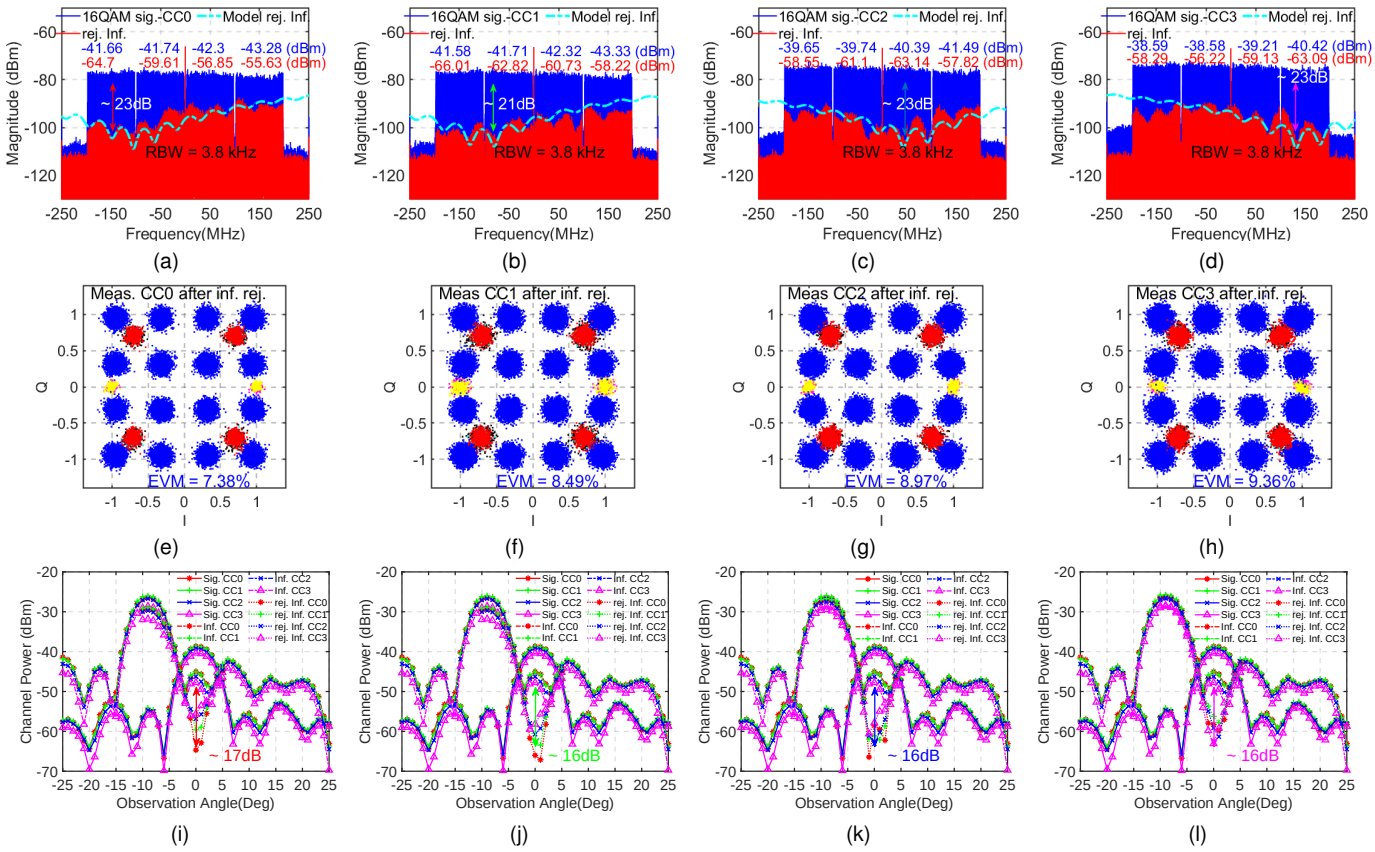

Fig. 19. (a)-(d) 5G NR 16 QAM 4CC signal and interference spectrum after interference cancellation one channel carrier at a time (CC0 - CC3) and measured spectrum after rejection are compared with OTA IBIC model simulations (e)-(h) CC0 - CC3 constellation respectively (i)-(l) signal and interferer beams with and without interference rejection (CC0 - CC3).

TABLE I
PERFORMANCE SUMMARY OF INTERFERENCE CANCELLING RECEIVERS AND COMPARISON

	JSSC'19 [Huang] [13]	JSSC'19 [Mondal] [12]	RFIC'16 [Jain] [15]	JSSC'17 [Zhang] [17]	JSSC'20 [Golabighezelahmad] [18]	This Work
Technology	45nm PDSOI	65nm	65nm	65nm	22nm FDSOI	45nm PDSOI
Receiver Architecture	single conv. to IF	Heterodyne, Dual stream	RF only	zero-IF	zero-IF	IF-RX[1] / zero-IF
Frequency RF (GHz)	27 – 41	27-29.75/ 35-38.75	9.3-10.3	0.1 - 3.1	0.7 - 5.7	27.9[1]
Frequency IF (GHz)	2.5-5	3.75-4.5	n/a	n/a	n/a	1.8 - 3.6[2]
BB Bandwidth	n/a	n/a	n/a	~ 10 MHz	100 MHz	**400MHz**
Power Consumption (mW)	85/ 1-LNA, mixer+3ASF	52/1-element	145/1-element	37 / 1-element	35 / 1-element	104/IF-RX
Active Area (mm^2)	~ 6.55/single stage	0.42/element	0.95/element	0.36/element/stream	0.13/element/stream	0.28/IF-RX
Signal Type	wideband SC	CW	CW	wideband SC	wideband SC	5GNR FR2 OFDM
Measurement	Conductive	Conductive	Conductive	OTA	Conductive*/ OTA#	OTA
Cancellation Technique	Arbitrary Spatial Filtering 3-stage	Null steering	Feed forward-cancellation	Freq. Translated-Spatial Notch Filter	Orthogonal beam	Spatial filter + IBIC
Modulated Signal BW (MHz)	100 256QAM 200, 500 64QAM	n/a	CW	2 QPSK	10*/ 1# 256QAM 100* 16QAM	50 64QAM 50, 100, 400 16QAM
Interferer type	Same as signal	CW	CW	CW	same as signal	**same as signal**
Number of Interferers	2	1	1	2	1*#	1
Signal at RX input (dBm)	-43	n/a	n/a	-68	-50	-50
Interferer level relative to desired signal (dB)	+3 and +8	n/a	n/a	+11	-5*/ -20# 256QAM +5* 16QAM	**+10**
Signal Data rates	0.8Gb/s 256QAM 1.2, 3Gb/s 64QAM	CW	CW	2Mb/s QPSK	80*/ 8# Mb/s 256QAM[7] 0.2Gb/s* 16QAM[7]	0.258Gb/s 64QAM[3] 0.353Gb/s[4] 16QAM[3]
Interferer offset from center frequency of desired signal	0.5 x Signal BW offset	40 MHz offset	n/a	0.6 MHz	No offset	**No offset**
EVM of signal after interference rejection (%)	2.3 256QAM[6] 2.3, 3.7 64QAM[6]	n/a	n/a	20.5	2*/ 1.6# 256QAM 8.9* 16QAM	6.5 64QAM 6.8 - 9 16QAM[5]
Interference rejection (dB)	32 - 36 256QAM[6] 32 - 36 64QAM[6]	20-25[8]	20[9] at 100 MHz notch BW	24	29*/15# 256QAM 27* 16QAM	**37** 64QAM[7] **34 - 37** 16QAM[7]

[1]-Tested with external mmWave subarrays, [2]- IF-RX only [3]- OFDM uncoded data rates [4]- Reported for single CC 100MHz, [5]- The EVM signal is in the following order: 50, 100, 100/CC BW signal, [6]- EVMs are in the same order as modulated signal BW, [7]- Spatial filtering plus improvement with IBIC up to 100 MHz BW, [8]- In carrier aggregation mode and using null steering only, * conductive measurements, # OTA measurements, n/a not available

cases, but they have not been tested OTA with wideband signals. Table I summarizes the performance of the IF-RX chip and rejection scheme and benchmarks it with state-of-the-art cancellation techniques. The interference rejection results include the spatial filtering of the external mmWave module in front of the IF-RX chips and IBIC. A comparison is made with mmWave wideband and multi-band [12], [13], RF front-end only [15], and sub-6-GHz [17], [18] receivers. The IF-RX achieved 1.8-GHz IF bandwidth, which is limited by external balun, and has the widest BB bandwidth of 400 MHz, making it suitable for wideband combining or interference rejection in mmWave 5G NR systems. Huang and Wang [13] covered most of the mmWave 5G NR band and has 2.5-GHz IF bandwidth but has the largest chip area per cancellation stage because wideband cancellation is achieved by creating delays with passive components at IF and mmWave. IF-RX chip has higher power consumption compared to others (single element) due to differential implementation and Cartesian combining function, which requires four differential gm stages in one slice.

Please note that we use realistic OTA measurement scenarios and do not use a frequency offset. This work achieves 34-37 dB interference rejection when IBIC operating as part of the mmWave system at the worst-case side lobe scenario. In spatial filtering with a uniform array, 18 dB comes from the array, and the rest comes from the IBIC. It shows the effectiveness of this architecture for wideband signals. On the other hand, Mondal and Paramesh [12], Huang and Wang [13] and Jain et al. [15] used conductive measurements for interference rejection, whereas Zhang et al. [16] used OTA and Golabighezelahmad et al. [18] used both OTA and conductive measurements. The measurements in [13], [17], [22] used frequency offset except [18]. However, conductive measurements show the wideband rejection but do not emulate the nonidealities of OTA channel, Golabighezelahmad [18] showed 27-dB of rejection over 100-MHz 16 QAM SC wideband signal cancellation in conductive measurements but only 15-dB rejection for 1-MHz 256 QAM SC signal in OTA measurements. Zhang and Krishnaswamy [17] used an 11-dB stronger CW interferer and showed 24-dB rejection. The conductive measurements of wideband rejection in [13] used passive delay lines at IF to match the delay differences between antenna elements. However, the rejection requires large angular separation, a minimum 3-dB power offset, and 50% frequency offset of the signal bandwidth.

The reported data rates of OFDM signals were estimated using 3GPP TS 38.306 standard signals with all the slots used for the downlink, and for other references, reported the theoretical limit. Standard signal configurations in 3GPP are not corresponding to the theoretical maximum for certain data rates. Therefore, the given numbers are indicative only and not directly comparable to ones without protocol overhead.

VII. Conclusion

This article presented a subarray based IF downconversion receiver architecture supporting hybrid beamforming for large-scale arrays with wideband IBIC. It utilizes both spatial rejection of mmWave subarrays and IBIC by rerotating the interfering beam to cancel the interference from another independent subarray. Subarrays also filter multipath reflections that cause frequency-dependent interference. However, even small reflections and RF nonidealities have a significant impact on cancellation properties of wideband signals. A theoretical OTA IBIC model with different nonidealities is analyzed and matched to OTA measurement results of the prototype receiver consisting of two mmWave subarrays and IF-RX chips providing IBIC. A two-phase calibration method to optimize the cancellation performance is utilized to achieve accurate and phase optimized cancellation coefficients.

It was demonstrated in the OTA measurements that a single IF-RX with an attenuator to adjust amplitudes in the cancellation path achieves 16-19-dB rejection over 100 MHz bandwidth signals. Furthermore, for wideband carrier-aggregated waveforms, it is shown that cancellation can be trained for each CC individually, and 16-dB rejection is achieved over 400 MHz multi-carrier 5G NR waveform. In contrast to many of the reported cancellers in the literature, our results are achieved for an interferer that is fully overlapping with the received data stream and realistic OTA signal conditions.

Acknowledgment

The authors would like to thank Global Foundries for providing silicon fabrication through the 45RFSOI university program and Keysight Technologies for the measurement equipment and 5G NR waveform support.

References

[1] W. Roh *et al*., "Millimeter-wave beamforming as an enabling technology for 5G cellular communications: theoretical feasibility and prototype results," *IEEE Commun. Mag*, vol. 52, no. 2, pp. 106–113, Feb. 2014.

[2] S. Jeon *et al*., "A scalable 6-to-18 GHz concurrent dual-band quad-beam phased-array receiver in cmos," *IEEE J. Solid-State Circuits*, vol. 43, no. 12, pp. 2660–2673, Jan. 2008.

[3] S. Shahramian, M. J. Holyoak, A. Singh, and Y. Baeyens, "A fully integrated 384-element, 16-tile, w-band phased array with self-alignment and self-test," *IEEE J. Solid-State Circuits*, vol. 54, no. 9, pp. 2419–2434, Aug. 2019.

[4] B. Sadhu *et al.*, "A 28-GHz 32-element TRX phased-array IC with concurrent dual-polarized operation and orthogonal phase and gain control for 5G communications," *IEEE J. Solid-State Circuits*, vol. 52, no. 12, pp. 3373–3391, Nov. 2017.

[5] K. Kibaroglu, M. Sayginer, and G. M. Rebeiz, "A low-cost scalable 32-element 28-GHz phased array transceiver for 5G communication links based on a 2×2 beamformer flip-chip unit cell," *IEEE J. Solid-State Circuits*, vol. 53, no. 5, pp. 1260–1274, Jan. 2018.

[6] T. Sowlati *et al*., "A 60-GHz 144-element phased-array transceiver for backhaul application," *IEEE J. Solid-State Circuits*, vol. 53, no. 12, pp. 3640–3659, Oct. 2018.

[7] A. Puglielli *et al*., "Design of energy- and cost-efficient massive MIMO arrays," *Proc. IEEE*, vol. 104, no. 3, pp. 586–606, Dec. 2016.

[8] R. W. Heath *et al*., "An overview of signal processing techniques for millimeter wave MIMO systems," *IEEE J. Sel. Topics Signal Process.*, vol. 10, no. 3, pp. 436–453, Apr. 2016.

[9] S. Dutta, C. N. Barati, D. Ramirez, A. Dhananjay, J. F. Buckwalter, and S. Rangan, "A case for digital beamforming at mmwave," *IEEE Trans. Wireless Commun.*, vol. 19, no. 2, pp. 756–770, Feb. 2020.

[10] M. Y. Javed, N. Tervo, and A. Pärssinen, "Inter-beam interference reduction in hybrid mmW beamforming transceivers," in *2018 IEEE 29th Annu. Int. Symp. Pers., Indoor Mobile Radio Commun. (PIMRC)*, Sep. 2018, pp. 220–224.

[11] H.-T. Kim *et al*., "A 28GHz CMOS direct conversion transceiver with packaged antenna arrays for 5G cellular system," in *Proc. IEEE Radio Freq. Integr. Circuits Symp. (RFIC)*, May, 2017, pp. 69–72.

[12] S. Mondal and J. Paramesh, "A reconfigurable 28-/37-GHz MMSE-adaptive hybrid-beamforming receiver for carrier aggregation and multi-standard MIMO communication," *IEEE J. Solid-State Circuits*, vol. 54, no. 5, pp. 1391–1406, Jan. 2019.

[13] M. Huang and H. Wang, "A Mm-Wave Wideband MIMO RX With Instinctual Array-Based Blocker/Signal Management for Ultralow-Latency Communication," *IEEE J. Solid-State Circuits*, vol. 54, no. 12, pp. 3553–3564, Oct. 2019.

[14] E. Naviasky, L. Iotti, G. LaCaille, B. Nikolić, E. Alon, and A. M. Niknejad, "A 71-to-86GHz packaged 16-Element by 16-Beam Multi-User Beamforming Integrated Receiver in 28nm CMOS," in *IEEE Int. Solid-State Circuits Conf. (ISSCC) Dig. Tech. Papers*, vol. 64, Feb. 2021, pp. 218–220.

[15] S. Jain, Y. Wang, and A. Natarajan, "A 10GHz CMOS RX frontend with spatial cancellation of co-channel interferers for MIMO/digital beamforming arrays," in *Proc. IEEE Radio Freq. Integr. Circuits Symp. (RFIC)*, May 2016, pp. 99–102.

[16] L. Zhang, A. Natarajan, and H. Krishnaswamy, "Scalable Spatial Notch Suppression in Spatio-Spectral-Filtering MIMO Receiver Arrays for Digital Beamforming," *IEEE J. Solid-State Circuits*, vol. 51, no. 12, pp. 3152–3166, Sep. 2016.

[17] L. Zhang and H. Krishnaswamy, "Arbitrary Analog/RF Spatial Filtering for Digital MIMO Receiver Arrays," *IEEE J. Solid-State Circuits*, vol. 52, no. 12, pp. 3392–3404, Nov. 2017.

[18] S. Golabighezelahmad, E. A. M. Klumperink, and B. Nauta, "A 0.7–5.7 GHz reconfigurable MIMO receiver architecture for analog spatial notch filtering using orthogonal beamforming," *IEEE J. Solid-State Circuits*, vol. 56, no. 5, pp. 1527–1540, Oct. 2021.

[19] M. A. Alaei *et al*., "Interference mitigation by adaptive analog spatial filtering for MIMO receivers," *IEEE Trans. Microw. Theory Techn.*, vol. 69, no. 9, pp. 4169–4179, Sep. 2021.

[20] C. Kim *et al*., "A 1.3 mW 48 MHz 4 channel MIMO baseband receiver with 65 dB harmonic rejection and 48.5 dB spatial signal separation," *IEEE J. Solid-State Circuits*, vol. 51, no. 4, pp. 832–844, Mar. 2016.

[21] R. Akbar *et al*., "A wideband IF receiver module for flexibly scalable mmwave beamforming combining and interference cancellation," in *ESSCIRC Conf.: 45th European Solid-State Circuits Conf.*, Sep. 2019, pp. 213–216.

[22] S. Mondal, R. Singh, A. I. Hussein, and J. Paramesh, "A 25-30 GHz 8-antenna 2-stream hybrid beamforming receiver for mimo communication," in *Proc. IEEE Radio Freq. Integr. Circuits Symp. (RFIC)*, May, 2017, pp. 112–115.

[23] R. Akbar, R. A. Shaheen, T. Rahkonen, C. Tze, K. Stadius, and A. Parssinen, "A 38.5-to-60.5 GHz LNA with wideband combiner supporting cartesian beamforming architecture," in *Proc. IEEE 47th European Solid State Circuits Conference (ESSCIRC)*, 2021, pp. 199–202.

[24] M. C. M. Soer, E. A. M. Klumperink, D.-J. van den Broek, B. Nauta, and F. E. van Vliet, "Beamformer with constant-gm vector modulators and its spatial intermodulation distortion," *IEEE J. Solid-State Circuits*, vol. 52, no. 3, pp. 735–746, Mar. 2017.

[25] M. C. M. Soer, E. A. M. Klumperink, B. Nauta, and F. E. van Vliet, "Spatial interferer rejection in a four-element beamforming receiver front-end with a switched-capacitor vector modulator," *IEEE J. Solid-State Circuits*, vol. 46, no. 12, pp. 2933–2942, Sep. 2011.

[26] R. K. Palani and R. Harjani, *"Inverter-Based Circuit Design Techniques for Low Supply Voltages,"*. Cham Switzerland: Springer, 2017.

[27] L. Sundstrom, M. Faulkner, and M. Johansson, "Effects of reconstruction filters in digital predistortion linearizers for RF power amplifiers," *IEEE Trans. Veh. Technol.*, vol. 44, no. 1, pp. 131–139, Feb. 1995.

[28] K. E. Kolodziej, B. T. Perry, and J. S. Herd, "In-band full-duplex technology: Techniques and systems survey," *IEEE Trans. Microw. Theory Techn.*, vol. 67, no. 7, pp. 3025–3041, Feb. 2019.

[29] R. Tseng, H. Li, D. H. Kwon, Y. Chiu, and A. S. Y. Poon, "A four-channel beamforming down-converter in 90-nm CMOS utilizing phase-oversampling," *IEEE J. Solid-State Circuits*, vol. 45, no. 11, pp. 2262–2272, Oct. 2010.

[30] Y. Cao and J. Zhou, "Integrated self-adaptive and power-scalable wideband interference cancellation for full-duplex MIMO wireless," *IEEE J. Solid-State Circuits*, vol. 55, no. 11, pp. 2984–2996, Nov. 2019.

[31] A. El Sayed *et al*., "A hilbert transform equalizer enabling 80 MHz RF self-interference cancellation for full-duplex receivers," *IEEE Trans. Circuits Syst. I, Reg. Papers*, vol. 66, no. 3, pp. 1153–1165, Mar. 2019.

[32] A. Nagulu *et al*., "A full-duplex receiver with true-time-delay cancelers based on switched-capacitor-networks operating beyond the delay–bandwidth limit," *IEEE J. Solid-State Circuits*, vol. 56, no. 5, pp. 1398–1411, May 2021.

[33] S. Golabighezelahmad, E. A. M. Klumperink, and B. Nauta, "EVM-based performance evaluation of co-channel interference mitigation using spatial filtering for digital MIMO receivers," in *2020 IEEE 92nd Vehicular Technology Conference (VTC2020-Fall)*, Nov. 2020, pp. 1–5.

[34] M. E. Leinonen, M. Jokinen, N. Tervo, O. Kursu, and A. Pärssinen, "System EVM characterization and coverage area estimation of 5G directive mmW links," *IEEE Trans. Microw. Theory Techn.*, vol. 67, no. 12, pp. 5282–5295, Dec. 2019.

[35] *NR Base Station (BS) Radio Transmission and Reception*. document TS 38. 104/2, 3GPP. V16.3.0 Release 16, Mar. 2020.

[36] M. Jokinen, O. Kursu, N. Tervo, J. Saloranta, M. E. Leinonen, and A. Pärssinen, "Over-the-air phase measurement and calibration method for 5G mmW phased array radio transceiver," in *in Proc. 93rd ARFTG Microw. Meas. Conf. (ARFTG), Boston, MA, USA*, Jun. 2019, pp. 1–4.

Rehman Akbar (Graduate Student Member, IEEE) received the M.Sc. degree in electrical engineering from Tampere University of Technology (TUT), Tampere, Finland, in 2014. From 2012 to July 2015, he was a member of the RFIC Design Lab at TUT, where he worked on VHF range DC-DC converters for mobile devices. He is currently pursuing a Ph.D. degree in electrical engineering at the University of Oulu, Oulu, Finland. Since 2022, he has been an Experienced Researcher with the Radio Architecture and Integration Systems Group, Ericsson Research, Ericsson, Lund. His research interests include the design of wideband RF/mmWave/BB integrated circuits, primarily in CMOS technology, radio architecture and integration for next-generation wireless systems.

Eric A. M. Klumperink (Fellow, IEEE) was born in Lichtenvoorde, The Netherlands, in 1960. He received the B.Sc. degree from HTS, Enschede, The Netherlands, in 1982. He worked in the industry on digital hardware and software, and then joined the University of Twente, Enschede, in 1984, shifting focus to analog CMOS circuit research. This resulted in several publications and his Ph.D. thesis was on "transconductance-based CMOS circuits: circuit generation, classification, and analysis" in 1997. In 1998, he started as an Assistant Professor at the IC-Design Laboratory, University of Twente, and shifted research focus to RF CMOS circuits (e.g., sabbatical at Ruhr-Universitäet Bochum, Bochum, Germany). Since 2006, he has been an Associate Professor with the University of Twente, teaching analog and RF IC electronics and guiding Ph.D. and M.Sc. projects related to RF CMOS circuit design with a focus on software-defined radio, cognitive radio, and beamforming. He holds several patents, authored and coauthored more than 175 internationally refereed journal articles and conference papers, and was recognized as more than 20 International Solid State Circuits Conference (ISSCC) Paper Contributor over 1954–2013.

Dr. Klumperink has served as the IEEE SSC Distinguished Lecturer from 2014 to 2015 and a Member of the Technical Program Committee of ISSCC from 2011 to 2016. He has been a Member of the Technical Program Committee of IEEE RFIC Symposium since 2011. He was a co-recipient of ISSCC 2002 and ISSCC 2009 "Van Vessem Outstanding Paper Award." He has also served as an Associate Editor for the IEEE TRANSACTIONS ON CIRCUITS AND SYSTEMS—II: EXPRESS BRIEFS (TCAS-II) from 2006 to 2007, IEEE TRANSACTIONS ON CIRCUITS AND SYSTEMS—I: REGULAR PAPERS (TCAS-I) from 2008 to 2009, and the IEEE JOURNAL OF SOLIDSTATE CIRCUITS (JSSC) from 2010 to 2014.

Nuutti Tervo (Member, IEEE) received the B.Sc. (Tech.), M.Sc. (Tech.), and D.Sc. (Tech.) degrees from the University of Oulu, Oulu, Finland, in 2014 and 2022, all with distinctions. His doctoral dissertation research focused on nonlinearity and linearization of millimeter-wave beamforming transceivers. Since 2022 he has been working as postdoctoral researcher at the Centre for Wireless Communications – Radio Technologies (CWC-RT) research unit in the University of Oulu.

He has a strong background in different fields of wireless communications, including radio frequency (RF), radio channel modeling, signal processing, and system-level analysis. Around those topics, he has already authored or coauthored more than 60 international journal and conference papers and he holds several patents. In 2019, he was a recipient of the Young Scientist Award of the URSI XXXV Finnish Convention on Radio Science, Tampere, and in 2020, he co-authored the paper that won the 50th EuMC Microwave Prize 2020, Utrecht, The Netherlands.

Kari Stadius (Member, IEEE) received the M.Sc., Lic. Tech., and Doctor of Science degrees in electrical engineering from the Helsinki University of Technology, Helsinki, Finland, in 1994, 1997, and 2010, respectively. He is currently working as a staff scientist at the Department of Electronics and Nanoengineering, Aalto University School of Electrical Engineering. His research interests include RF and microwave circuits for communications, and analog and mixed-mode circuit design. He has authored or coauthored over a hundred refereed journal and conference papers, and he holds several patents.

Timo Rahkonen (Member, IEEE) was born in Jyvaskylä, Finland, 1962. He received the Diploma, Licentiate, and Doctor of Technology degrees from the University of Oulu, Oulu, Finland, in 1986, 1991, and 1994, respectively.

He is currently a Professor of circuit theory and circuit design with the University of Oulu, conducting research, especially in linearization and distortion analysis. His current research interests include 28- and 300-GHz band transceiver IC development.

Aarno Pärssinen (Senior Member, IEEE) received the M.Sc., Licentiate in Technology, and D.Sc. degrees in electrical engineering from the Helsinki University of Technology, Helsinki, Finland, in 1995, 1997, and 2000, respectively. From 1994 to 2000, he was with the Electronic Circuit Design Laboratory, Helsinki University of Technology, working on direct conversion receivers and subsampling mixers for wireless communications. In 1996, he was a Research Visitor at the University of California at Santa Barbara, Santa Barbara, CA, USA. From 2000 to 2011, he was with the Nokia Research Center, Helsinki. From 2009 to 2011, he served as a member for the Nokia CEO Technology Council. From 2011 to 2013, he was at Renesas Mobile Corporation, Helsinki, working as a Distinguished Researcher and the RF Research Manager. From October 2013 to September 2014, he was an Associate Technical Director at Broadcom, Helsinki. Since September 2014, he has been with the Centre for Wireless Communications, University of Oulu, Oulu, Finland, where he is currently a Professor. He leads the devices and circuits research area in the 6G flagship program financed by the Academy of Finland. He has authored and coauthored one book, two book chapters, more than 200 international journals and conference papers, and holds several patents. His research interests include wireless systems and transceiver architectures for wireless communications with special emphasis on RF and analog integrated circuits and system design.

Dr. Pärssinen was a recipient of the European Microwave Prize on the Best Paper of the European Microwave Conference in 2020. He is also one of the original contributors to Bluetooth low energy extension, now called BT LE. He served as a member for the Technical Program Committee of the International Solid-State Circuits Conference from 2007 to 2017, where he was the Chair of the European Regional Committee from 2012 to 2013 and the Wireless Sub-Committee from 2014 to 2017. He has been serving as Solid-State Circuits Society Representative for IEEE 5G initiative from 2015 to 2019.